Three-dimensional numerical modeling of natural convection in underground cavities connected to the surface by a well

Georges Edde, Georges Sadaka, Raphaël Antoine, Ionut Danaila

Three-dimensional numerical modeling of natural convection in underground cavities connected to the surface by a well

Georges Edde[1,2], Georges Sadaka[2], Raphaël Antoine[1] and Ionut Danaila[2,*]

[1]ENDSUM-Rouen team, Cerema, 10 Chemin de la Poudrière,
76120, Le Grand-Quevilly, France.
[2]Univ Rouen Normandie, CNRS, Laboratoire de Mathématiques Raphaël Salem,
UMR 6085, F-76000 Rouen, France
* Corresponding author: ionut.danaila@univ-rouen.fr

September 18, 2024

Abstract

We present two- and three-dimensional numerical simulations of the natural convection flow within an artificial underground cavity. We consider a realistic geometry reconstructed from measurements (3D point cloud obtained with a photogrammetric method) of the Barcq cavity existing in Normandy region, France. The numerical model solves the Navier-Stokes equations coupled with the unsteady heat equation using a finite-element method for the space discretization. Time integration is based on a semi-implicit method and the Newton method to solve the resulting non-linear equation. To implement the method, we use the free software FreeFem++ offering efficient mesh refinement/adaptivity tools. The parallelization of the simulations relies upon the `PETSc` software library, to which FreeFem++ offers an easy-to-use interface. We analyze the onset of the natural convection and characterize the convective cells developing within the Barcq cavity for five Rayleigh ($\mathcal{R}a$) numbers (from 10^5 to 10^9). Dimensionless temperatures, velocities and Nusselt numbers are presented for each Ra number. We discuss how these results can be used to understand the thermal behavior of small artificial cavities. We address in particular the influence of the value of the Rayleigh number on the flow inside the well, which is essential for designing detection methods based on surface temperature observations.

1 Introduction

Underground cavities of anthropogenic or natural origin are often undetected. Their erosion can lead to land subsidence and may generate sinkholes, threatening people, buildings and infrastructures. Underground cavities can be related to natural environments such as karsts and thus induce collapse processes in soluble rocks like limestone, salt or gypsum, but

also to man-made structures like quarries, cellars, sewers and tunnels. Sinkholes occur in Europe, USA, Saudi Arabia (Youssef et al., 2020), or South Korea (Lee et al., 2016) and thus represent an important threat worldwide. Besides, in the context of climate change, modifications in precipitations and temperature also have an impact on the stability of underground cavities, due to the increased variability of soil water content (Xiao et al., 2016). The early detection of cavities is thus of particular importance for public and infrastructure safety.

Geophysical imaging methods are usually used to detect underground cavities, such as micro-gravimetry (Closson et al., 2005), ground penetrating radar (GPR) (Kruse et al., 2006), electrical methods (Carbonel et al., 2014), seismic methods (Tran et al., 2013) or radar interferometry (Kulshrestha et al., 2021). Very recently, cosmic ray muons detectors (Saracino et al., 2017) were successfully used to detect hidden cavities in the great pyramid of Kheops in Egypt (Morishima et al., 2017). In situ, the choice of the method depends on the nature of the soil encountered, the complexity of the topography and the degree of urbanization. Eventually, in situ drilling complete the measurements to confirm the observed geophysical anomalies (Philippe et al., 2022).

Experiments have also been conducted with aerial remote sensing techniques to detect underground cavities or sinkholes. Laser technology (namely LiDAR) and photogrammetric methods are two techniques used to identify potential subsurface cavities by assessing the surface geometry of the soil (Benito-Calvo et al., 2018; Antoine et al., 2020). Near infrared imagery can also be helpful to investigate the presence of subsurface cavities through variations in vegetation activity and soil reflectance (Cooper, 1989). The thermal infrared method (TIR) provides measurements of the surface temperature. This technique was particularly successful to detect caves (Wynne et al., 2008), shallow caves ducts (Perez-Garcia et al., 2018), buried pipes (Carreño-Alvarado et al., 2014), sinkholes (Lee et al., 2016) and lava tubes (Lopez et al., 2012).

In the 2000s, numerous remote sensing experiments were performed in the Normandy region, known to have an important density of artificial cavities (10 per km^2). Such structures are located several meters/tens of meter underground and are connected to the surface by a 1m-diameter well. They are usually small (few m^3 to tens of m^3), empty, and their wells may be filled (or not) with rough materials (Adam et al., 2008). Their collapse thus represents a serious hazard for people and infrastructures. Aerial thermal data made it possible to detect the thermal signature of several buried wells (Fauchard and Pothérat, 2004; Adam et al., 2008). Temperature contrasts of several degrees Celsius were detected between the wells and their surrounding environment by TIR cameras, making this method promising for future detection, in particular when the wells are buried within the soil (invisible from the surface). To our knowledge, the physical processes at the origin of these observations have never been investigated and represent a challenge for the development of detection methodologies. Numerical modeling of the heat and mass transfer between the atmosphere and underground cavities is crucial and may constitute an interesting approach to perform sensitivity studies and understand how thermal anomalies develop in such structures.

The objective of the present work is to develop a numerical system that is efficient and easy-to-use for simulating the thermal behavior of a realistic artificial cavity fully connected to the atmosphere by a well. We take into account the transport of air and the heat transfer associated with this flow, relative to temperature and pressure gradients,

which are known to influence the subsurface cavity micrometeorology (Buecher et al., 1999; Wilson et al., 2008). We also consider a realistic three-dimensional (3D) geometry obtained in situ using the photogrammetric method. Previous studies (Wigley and Brown, 1971; Dwivedi, 2010) emphasized the importance of the morphology of the cavity on the flow patterns and temperature gradients

The structure of the paper is as follows. In Sec. 2 we describe and validate against academic tests the finite-element method developed to simulate natural convection flows in cavities. Numerical simulations using the actual (Barcq) cavity geometry are presented in Section 3. We show 2D and 3D results and discuss the influence of main parameters on the flow morphology. Finally, the main features of the study are summarized in Sec. 4, where we additionally offer some of its potential extensions.

2 Modeling of natural convection flows in cavities

Natural convection is the spontaneous fluid motion that arises when variations in temperature cause denser, cooler fluid to sink while lighter, warmer fluid rises, creating a natural circulation pattern. Natural convection (driven only by the buoyancy force) becomes forced convection when additional external forces act on the fluid.

2.1 Mathematical model

In natural convection, fluid mechanics and heat transfer equations are strongly coupled and must be solved in the same time. We consider the motion of the air flow generated inside a closed domain Ω by the temperature difference $\delta T = T_{hot} - T_{cold}$ between a hot and a cold wall. We use the following system of equations, written in the dimensionless form:

$$\nabla \cdot \mathbf{u} = 0, \tag{1}$$

$$\frac{\partial \mathbf{u}}{\partial t} + (\mathbf{u} \cdot \nabla)\mathbf{u} + \nabla p - \frac{1}{\mathcal{R}e}\nabla^2 \mathbf{u} - f_B(\theta)\,\mathbf{e}_y = 0, \tag{2}$$

$$\frac{\partial \theta}{\partial t} + \nabla \cdot (\theta \mathbf{u}) - \frac{1}{\mathcal{R}e\mathcal{P}r}\nabla^2 \theta = 0, \tag{3}$$

Equations (1) and (2) are the Navier-Stokes equations describing the motion of the fluid of an incompressible flow (conservation of mass and momentum, respectively). Buoyancy effects are modeled using the Boussinesq approximation, assuming that the density of the fluid is constant ($\rho = \rho_0$) in all equations, excepting the expression of the buoyancy force f_B (see below). Equation (3) is the energy conservation equation, written in the form of an advection-diffusion equation for the temperature.

In Eqs. (1)-(3), non-dimensional space $\mathbf{x}$, velocity $\mathbf{u}$, temperature θ, pressure p and time t variables were obtained from physical ones after applying the following scaling:

$$\mathbf{x} = \frac{\mathbf{X}}{H}\,,\ \mathbf{u} = \frac{\mathbf{U}}{V_{ref}}\,,\ \theta = \frac{T - T_{ref}}{\delta T}\,,\ p = \frac{P}{\rho_0 V_{ref}^2}\,,\ t = \frac{t_\varphi}{H/V_{ref}}, \tag{4}$$

where H, V_{ref} and T_{ref} are length, velocity and temperature reference values. The reference length H is usually the height of the cavity. Temperature difference δT defines

a temperature scale, and T_{ref} can be taken as either $T_{ref} = T_{cold}$ (*i. e.* $0 \leq \theta \leq 1$) or $T_{ref} = (T_{cold} + T_{hot})/2$ (*i. e.* $-1/2 \leq \theta \leq 1/2$).

Using the general scaling (4), the following expressions are obtained for the Reynolds ($\mathcal{R}e$) and Prandtl ($\mathcal{P}r$) numbers:

$$\mathcal{R}e = \frac{V_{ref} H}{\nu}, \quad \mathcal{P}r = \frac{\nu}{\alpha}, \tag{5}$$

where ν is the kinematic viscosity and α the thermal diffusivity of the fluid. The Boussinesq force f_B is obtained by linearizing the density variation $\rho(\theta)$ in the expression of the buoyancy force:

$$f_B(\theta) = \frac{\mathcal{R}a}{\mathcal{P}r\mathcal{R}e^2}\theta, \tag{6}$$

where the Rayleigh ($\mathcal{R}a$) number is defined as:

$$\mathcal{R}a = \frac{g\beta H^3 \delta T}{\nu\alpha}, \tag{7}$$

with β the thermal expansion coefficient and g the gravitational acceleration. For natural convection problems, it is common to simplify the expression of the Boussinesq force by choosing a particular velocity scale:

$$V_{ref} = \frac{\nu}{H}\sqrt{\frac{\mathcal{R}a}{\mathcal{P}r}} \Longrightarrow \mathcal{R}e = \sqrt{\frac{\mathcal{R}a}{\mathcal{P}r}} \Longrightarrow f_B(\theta) = \theta. \tag{8}$$

Note that our numerical system is written using the general scaling (4). For the natural convection simulation presented in this paper, we apply the particular choice (8) for the velocity scale.

2.2 Numerical model

Finite-element methods for solving Navier-Stokes type systems of equations are generally based on a separate discretization of the temporal derivative (using finite differences, splitting or characteristics methods) and the generalization of the Stokes problem for the resulting system (Temam, 1983; Girault and Raviart, 1986; Quarteroni and Valli, 1994). Note that a more general form of the system of equations (1)-(3), including liquid-solid phase change, was solved recently using sequential algorithms in (Rakotondrandisa et al., 2020) and parallel finite element algorithms in (Sadaka et al., 2020).

We use for this study a time integration method based on the second-order Gear (BDF2) finite-difference scheme (see also Belhamadia et al., 2012):

$$\frac{d\eta}{dt} \simeq \frac{3\eta^{n+1} - 4\eta^n + \eta^{n-1}}{2\delta t} = c_1\eta^{n+1} + c_2\eta^n + c_3\eta^{n-1}. \tag{9}$$

The solution η^{n+1} at time instant $t^{n+1} = (n+1)\delta t$ is thus computed by using two previous states (η^n, η^{n-1}). We use this scheme to advance in time both velocity ($\eta = \mathbf{u}$) and

temperature fields ($\eta = \theta$). The other terms in equations (1)-(3) are treated implicitly. We obtain the following implicit semi-discretization in time:

$$\nabla \cdot \mathbf{u}^{n+1} + \gamma p^{n+1} = 0, \quad (10)$$

$$c_1 \mathbf{u}^{n+1} + (\mathbf{u}^{n+1} \cdot \nabla)\mathbf{u}^{n+1} + \nabla p^{n+1} - \frac{1}{\mathcal{R}e}\nabla^2 u^{n+1} - f_B(\theta^{n+1})\,\mathbf{e}_y + c_2 \mathbf{u}^n + c_3 \mathbf{u}^{n-1} = 0, \quad (11)$$

$$c_1 \theta^{n+1} + \nabla \cdot \left(\mathbf{u}^{n+1}\theta^{n+1}\right) - \frac{1}{\mathcal{R}e\mathcal{P}r}\nabla^2 \theta^{n+1} + c_2 \theta^n + c_3 \theta^{n-1} = 0. \quad (12)$$

Note that we introduced in Eq. (10), which is the discrete version of the mass conservation equation (1), a penalty term using the pressure. This term will provide a regularization of the solution by ensuring a pressure field with zero average and, at the algebraic level, filling the diagonal of the pressure term (see Legrand et al., 2023). Compared to classical penalty methods, we use here a very low value $\gamma = 10^{-7}$ for the penalty parameter.

To solve the system of equations (10)-(12) we use a classical Galerkin finite-element method. We consider homogeneous Dirichlet boundary conditions for the velocity, *i. e.* $\mathbf{u} = 0$ on $\partial\Omega$. As a consequence, we set the following Hilbert spaces for the velocity and pressure:

$$\mathbf{V} = V \times V,\ V = H_0^1(\Omega), \quad Q = \left\{ q \in L^2(\Omega) \;\middle|\; \int_\Omega q = 0 \right\}. \quad (13)$$

Following the generalization of the Stokes problem Temam (1983); Girault and Raviart (1986); Quarteroni and Valli (1994), the weak formulation of the system (10)-(12) can be written after integrating by parts as: find $(\mathbf{u}^{n+1}, p^{n+1}, \theta^{n+1}) \in \mathbf{V} \times Q \times V$, such that:

$$b\left(\mathbf{u}^{n+1}, q\right) - \gamma(p^{n+1}, q) = 0, \quad \forall\, q \in Q, \quad (14)$$

$$\left(c_1 \mathbf{u}^{n+1}, \mathbf{v}\right) + c\left(\mathbf{u}^{n+1}; \mathbf{u}^{n+1}, \mathbf{v}\right) + \frac{1}{\mathcal{R}e}\, a\left(\mathbf{u}^{n+1}, \mathbf{v}\right) + b\left(\mathbf{v}, p^{n+1}\right)$$
$$-\left(f_B(\theta^{n+1})\,\mathbf{e}_y, \mathbf{v}\right) + \left(c_2 \mathbf{u}^n, \mathbf{v}\right) + \left(c_3 \mathbf{u}^{n-1}, \mathbf{v}\right) = 0, \quad \forall\, \mathbf{v} \in \mathbf{V}, \quad (15)$$

$$\left(c_1 \theta^{n+1} + \mathbf{u}^{n+1} \cdot \nabla \theta^{n+1}, \varphi\right) + \frac{1}{\mathcal{R}e\mathcal{P}r}\left(\nabla \theta^{n+1}, \nabla \varphi\right) - \frac{1}{\mathcal{R}e\mathcal{P}r}\left(\frac{\partial \theta^{n+1}}{\partial n}, \varphi\right)_1$$
$$+\left(c_2 \theta^n + c_3 \theta^{n-1}, \varphi\right) = 0, \quad \forall\, \varphi \in V, \quad (16)$$

where $(u, v) = \displaystyle\int_\Omega u \cdot v$ denotes the scalar product in $L^2(\Omega)$ or $\left(L^2(\Omega)\right)^2$, $(u, v)_1 = \displaystyle\int_{\partial\Omega} u \cdot v$; the bilinear forms a, b and trilinear form c are defined as (Girault and Raviart, 1986; Quarteroni and Valli, 1994):

$$a : \mathbf{V} \times \mathbf{V} \to \mathbb{R}, \qquad a(\mathbf{u}, \mathbf{v}) = \int_\Omega \nabla^{\mathbf{t}}\mathbf{u} : \nabla \mathbf{v} = \sum_{i,j=1}^{2} \int_\Omega \partial_j u_j \cdot \partial_j v_i,$$

$$b : \mathbf{V} \times Q \to \mathbb{R}, \qquad b(\mathbf{u}, q) = -\int_\Omega \nabla \cdot \mathbf{u}\, q = -\sum_{i=1}^{2} \int_\Omega \partial_i \mathbf{u}_i \cdot q,$$

$$c : \mathbf{V} \times \mathbf{V} \times \mathbf{V} \to \mathbb{R}, \qquad c(\mathbf{w}; \mathbf{z}, \mathbf{v}) = \int_\Omega \left[(\mathbf{w} \cdot \nabla)\,\mathbf{z}\right] \cdot \mathbf{v} = \sum_{i,j=1}^{2} \int_\Omega w_j (\partial_j z_i) v_i.$$

For the space discretization of the system (14)-(16) it is important to use for the velocity and pressure finite-elements that are stable (*i. e.* satisfy the inf-sup condition). Generally, Taylor-Hood (*i. e.* P_2 for the velocity and temperature and P_1 for the pressure) finite elements are preferred (see Rakotondrandisa et al., 2020; Sadaka et al., 2020), since they offer stability and quadratic accuracy. Another possible choice is the mini-element introduced by Arnold, Brezzi and Fortin (see Arnold et al., 1984; Brezzi and Fortin, 1991): the P_1 piecewise linear approximation functions are enriched with a bubble function (*i. e.* vanishing on the edges of the element) using an inner point (the barycenter). This is the simplest element for Stokes-type problems, offering inf-sup stability and global linear convergence. To save computational time, we use in this work the mini-element P_1^b (P_1-bubble) for velocities and P_1 for the pressure. For the temperature, we use either P_1 or P_2 finite elements. Note that FreeFem++ offers the possibility to use a large variety of finite elements. It is very easy to switch from one finite element to another by changing only one line in the script, that defining the finite element space. The corresponding definitions of the discrete spaces we used in this work are the following: P_{1b} for the velocity ($\mathbf{V}_h$ space), P_1 for the pressure (Q_h space) and P_1 or P_2 for the temperature (V_h space):

$$\mathbf{V}_h = \left\{ \mathbf{v} \in H^1(\Omega)^2 \;\middle|\; \forall K \in \mathcal{T}_h, \mathbf{v}_K \in \left(P_1 \oplus Span\{\lambda_0^K \lambda_1^K \cdots \lambda_d^K\} \right)^d \right\}, \tag{17}$$

$$Q_h = \left\{ v \in H^1(\Omega) \;\middle|\; \forall K \in \mathcal{T}_h, \quad v_{|K} \in P_1 \right\}, \tag{18}$$

$$V_h = \left\{ v \in H^1(\Omega) \;\middle|\; \forall K \in \mathcal{T}_h, \quad v_{|K} \in P_1 \text{ or } P_2 \right\}, \tag{19}$$

where $\lambda_i^K, i = 0, \cdots, d$ are the $d+1$ barycentric coordinate functions of the element K of the triangulation $\mathcal{T}_h$, where $d = 2, 3$ is the space dimension. The characteristic mesh size is denoted by h.

The implicit time-discretization resulted in the non-linear system of equations (14)-(16). To apply Newton's method, we write this system as $\mathcal{F}(w) = 0$, with $w = (\mathbf{u}^{n+1}, p^{n+1}, \theta^{n+1}) \in \mathbf{W} = \mathbf{V} \times Q \times V$ and $\mathcal{F} : \mathbf{W} \to \mathbf{W}$ a differentiable mapping. The classical Newton algorithm is then used to advance the solution from time t_n to t_{n+1}: starting from an initial guess $w_0 = (\mathbf{u}^n, p^n, \theta^n)$ (which is the solution at t_n), construct Newton sequence $w_k = (\mathbf{u}_k, p_k, \theta_k)$ by solving for each inner iteration k:

$$D_w \mathcal{F}(w_k)(w_k - w_{k+1}) = \mathcal{F}(w_k), \tag{20}$$

where $D_w \mathcal{F}$ is the linear operator representing the differential of $\mathcal{F}$. Denoting by $(\mathbf{u}_w, p_w, \theta_w) = w_k - w_{k+1}$ and after differentiating (14)-(16), the system of equations (20) can be explicitly

written as:

$$
\begin{aligned}
b\left(\mathbf{u}_w, q\right) - \left(\gamma p_w, q\right) &= b\left(\mathbf{u}_k, q\right) - \left(\gamma p_k, q\right), && (21)\\
\left(c_1 \mathbf{u}_w, \mathbf{v}\right) + c\left(\mathbf{u}_w; \mathbf{u}_k, \mathbf{v}\right) &+ c\left(\mathbf{u}_k; \mathbf{u}_w, \mathbf{v}\right)\\
+\frac{1}{\mathcal{R}e}\, a\left(\mathbf{u}_w, \mathbf{v}\right) + b\left(\mathbf{v}, p_w\right) - \left(\frac{df_B}{d\theta}(\theta_k)\, \theta_w\, \mathbf{e}_y, \mathbf{v}\right) &= \left(c_1 \mathbf{u}_k + c_2 \mathbf{u}^n + c_3 \mathbf{u}^{n-1}, \mathbf{v}\right)\\
+b\left(\mathbf{v}, p_k\right) + \frac{1}{\mathcal{R}e}\, a\left(\mathbf{u}_k, \mathbf{v}\right) &+ c\left(\mathbf{u}_k; \mathbf{u}_k, \mathbf{v}\right) - \left(f_B(\theta_k)\, \mathbf{e}_y, \mathbf{v}\right), && (22)\\
\left(c_1 \theta_w + \left(\mathbf{u}_w \cdot \nabla \theta_k + \mathbf{u}_k \cdot \nabla \theta_w\right), \varphi\right) + \left(\frac{1}{\mathcal{R}e\mathcal{P}r} \nabla \theta_w, \nabla \varphi\right) &- \left(\frac{1}{\mathcal{R}e\mathcal{P}r} \frac{\partial \theta_w}{\partial n}, \varphi\right)_1\\
= \left(c_1 \theta_k + \mathbf{u}_k \cdot \nabla \theta_k + c_2 \theta^n + c_3 \theta^{n-1}, \varphi\right) - \left(\frac{1}{\mathcal{R}e\mathcal{P}r} \frac{\partial \theta_k}{\partial n}, \varphi\right)_1 &+ \left(\frac{1}{\mathcal{R}e\mathcal{P}r} \nabla \theta_k, \nabla \varphi\right). && (23)
\end{aligned}
$$

The Newton loop (following k) has to be iterated until convergence for each time step δt following the algorithm:

$$
\begin{array}{l}
\text{set } w_0 = (\mathbf{u}^n, p^n, \theta^n)\\
\quad \text{Newton iterations following } k\\
\quad\quad \text{solve (21)-(23) to get } (\mathbf{u}_w, p_w, \theta_w)\\
\quad\quad \text{actualize } w_{k+1} = w_k - (\mathbf{u}_w, p_w, \theta_w)\\
\quad \text{stop when } \|(\mathbf{u}_w, p_w, \theta_w)\| < \xi_N\\
\text{actualize } (\mathbf{u}^{n+1}, p^{n+1}, \theta^{n+1}) = w_{k+1},
\end{array}
\qquad (24)
$$

where the tolerance ξ_N is usually set to $\xi_N = 10^{-10}$.

We present in Appendix A the space and time convergence rates, estimated using manufactured solutions. This technique (*e. g.* Roache (1998)) consists in modifying the original system of equations by introducing an extra source term, such that the new system admits an exact solution given by a convenient analytic expression. Exact solutions constructed in this way are not always physically realistic, but this approach allows one to rigorously verify computations. The results presented in Appendix A show the expected orders of accuracy: for the space accuracy we obtain first order ($\mathcal{O}(h)$) convergence for velocity and first or second order ($\mathcal{O}(h^2)$) convergence for the temperature (depending if P_1 or P_2 are used); for the time accuracy, the method is proved to be second order in time ($\mathcal{O}(\delta t^2)$).

3 Numerical simulation of natural convection inside the Barcq cavity

To test our code on a realistic domain, we consider the artificial cavity located at Barcq town in Normandy, France.

3.1 Mesh generation and adaptive mesh refinement

The geometry of the cavity was obtained in situ using the photogrammetric method: it consists in generating 3D points of the contour of an object using photographs taken from

different angles. This method offers a cost-effective and non-contact method for creating accurate 3D models (Fauchard et al., 2013).

Starting from the 3D-points cloud, we combined different numerical tools from (`Meshlab`[1], `open3d`[2], `Python`[3], `Gmsh`[4], `Freefem++`[5] and finally `Gimp`[6]) to generate 3D and 2D meshes shown in Fig. 1. These initial meshes are dynamically adapted/refined during the simula-

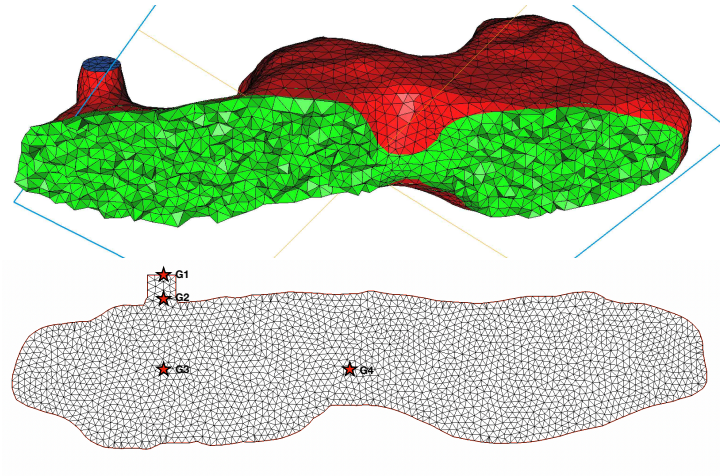

Figure 1: Initial finite element meshes generated using the 3D-points cloud from photogrammetric measurements: (up) full 3D mesh (tetrahedra) and (down) 2D mesh (triangles). The 2D mesh is the graphical parallel projection of the 3D mesh on the meridian plane. Gauges G1, G2, G3 and G4 are also represented on the 2D mesh.

tion (every time step in 2D). For the 2D geometry, we use the standard function (`adaptmesh`) which is a very convenient tool offered by FreeFem++ to efficiently adapt 2D meshes by metrics control (Hecht, 2012). The key idea implemented in this function is to modify the scalar product used in the automatic mesh generator to evaluate distance and volume. The scalar product is based on the evaluation of the Hessian $\mathcal{H}$ of the variables of the problem. A new mesh with equilateral elements is thus generated using the new metric. This algorithm is very fast and can be used to refine the mesh every time step. For the cases presented in this paper, the mesh was adapted using the values of the two velocity components and the temperature. As a consequence, the mesh density was increased in regions of high velocity or temperature gradients, depending on the value of the Rayleigh number (see below). For 3D simulations, we used similar mesh refinement algorithms implemented

[1] `https://www.meshlab.net`
[2] `https://github.com/isl-org/Open3D`
[3] `https://www.python.org/`
[4] `https://gmsh.info//`
[5] `https://freefem.org`
[6] `https://www.gimp.org`

in the libraries `mshmet` and `mmg` (Dapogny et al., 2014) to which FreeFem++ provides an easy-to-use interface.

3.2 Boundary and initial conditions

The flow inside the Barcq cavity is simulated by solving the system of equations (21)-(23) with boundary conditions as follows.

- We impose homogeneous Dirichlet boundary conditions on the velocity ($\mathbf{u} = 0$) on all walls (*i. e.* the surface of the well is also a wall).
- For the other underground walls of the cavity, we impose the value of the temperature (Dirichlet boundary conditions), assuming the following variation with the depth y of the cavity:
$$T_{wall}(y) = \frac{T_B - T_A}{y_B - y_A}(y - y_A) + T_A, \quad T_A > T_B, \tag{25}$$
where B the highest point of the cavity (*i. e.* $y_B = \max(y)$), corresponding to the position of the gauge G_1 in Fig. 1). Point A is the lowest point of the cavity (*i. e.* $y_A = \min(y)$).
- At the surface of the well ($y = y_B$), the temperature is also imposed and varies in time as:
$$T_{well}(t) = T_B \cos\left(2\pi \frac{t}{\lambda}\right). \tag{26}$$
This enables important variations of the temperature ($\delta T_{well} = 2T_B$) over the period λ. Note that initially (at $t = 0$) $T_{well}(t) = T_B$, which is a necessary condition for a proper start of the simulation.
- By taking
$$T_{ref} = (T_B + T_A)/2, \quad \delta T = T_A - T_B, \tag{27}$$
the nondimensional temperature θ (see Eq. (4)) in the whole underground domain will vary from 0.5 (at the bottom) to -0.5 (at the top). For a graphical representation of the time variation of the nondimensional temperature at the surface of the well (corresponding to the gauge G_1), see Fig. 5a below.

All simulations start from a initial condition modeling the fluid at rest: at $t = 0$, $\mathbf{u} = 0$, $\theta = 0$ (*i. e.* $T = T_{ref}$).

3.3 Results and discussion

The (2D and 3D) simulations presented in this section are performed on parallel computers using the interface of FreeFem++ with `PETSc`[7] open source library (Balay et al., 2022) (Portable, Extensible Toolkit for Scientific Computation). The details of the selected `PETSc` solvers for linear systems, necessary computational resources (CPU time, memory, number of processors, size of the mesh, etc.) and code performance are provided in Appendix B.

[7] `https://www.mcs.anl.gov/petsc/`

The key parameter in allotting computational resources is the Rayleigh number. Considering g, β, ν and α as constants, $\mathcal{R}a$ is dependent of the volume H^3 and δT (see Eq. (7)). For instance, taking values of H^3 in the range [10-100] m^3 and δT as low as $0.1°$, the $\mathcal{R}a$ number ranges from 10^8 to 10^9. To explore all possible regimes of natural convection in the cavity, we show in this section results for five values or the Rayleigh number: $\mathcal{R}a = 10^5, 10^6, 10^7, 10^8, 10^9$. Simulations are covering an entire time period λ for the oscillation of the boundary condition at the surface of the well (see Eq. 26).

For high values of the Ra number the velocity gradients at walls become more intense and thus need higher mesh resolutions. These cases are computationally challenging, since the dynamical mesh refinement rapidly results in a very dense mesh. For the cases presented below, we preferred to keep the high accuracy of the simulation instead of coarsening the mesh. This explains why the most difficult case, the 3D simulation for $\mathcal{R}a = 10^9$ was stopped before reaching the final time $t_f = \lambda = 50$.

3.3.1 Results for the 2D configuration

We start by analyzing the topology of the natural convection flow by presenting the velocity vectors in Fig. 2. The velocity magnitude increases from 0.2 for $\mathcal{R}a = 10^5$ (Fig. 2a) to 0.5 for $\mathcal{R}a = 10^9$ (Fig. 2e).

Surprisingly, the number of convective 2D cells remain quasi-constant as $\mathcal{R}a$ increases (5-7 major cells observed). This implies that the heat transfer is not enhanced by the multiplication of the number of convection cells, but rather by an increase of velocity gradients, mainly close to the walls (see the red regions in Fig. 2). For $\mathcal{R}a = 10^8$ and 10^9, we notice the fragmentation of large convection cells in smaller structures, indicating the transition towards a turbulent flow. Starting with $\mathcal{R}a = 10^7$, a recirculating convective flow becomes noticeable in the well of the cavity.

The observation on velocity fields correlate well with the temperature contours displayed in Fig. 3. As $\mathcal{R}a$ increases, the temperature gradient become stronger as the upward/downward plumes become thinner. We note that temperature gradients considerably increase in some areas and in particular within the well, where the movements are very rich due to the presence of upward/downward plumes with different shapes (Fig. 3 panels c-e) corresponding to recirculating flows seen in Fig. 2 (panels c-e). We infer that complex cold or hot temperature anomalies may be induced within the well. For $\mathcal{R}a = 10^7$, a cold plume is triggered at the top of the well, inducing the movement of an upward flow. A flow with increased complexity is observed for $\mathcal{R}a = 10^8$, where the generation of a hot upward flow at the left wall of the well is balanced by a cold downward flow at the right wall.

To illustrate how the adaptive mesh refinement follows the evolution of the increasing complexity of the flow with the $\mathcal{R}a$ number, we show in Fig. 4 the adapted meshes for the final time $t_f = 50$. The mesh is denser in regions of high velocity and temperature gradients (at the walls and also at the interface between convection cells). The maximum number of the degrees of freedom varies from 85 226 for $\mathcal{R}a = 10^8$ to 117 240 for $\mathcal{R}a = 10^9$ (see Tab. 1 in Appendix B).

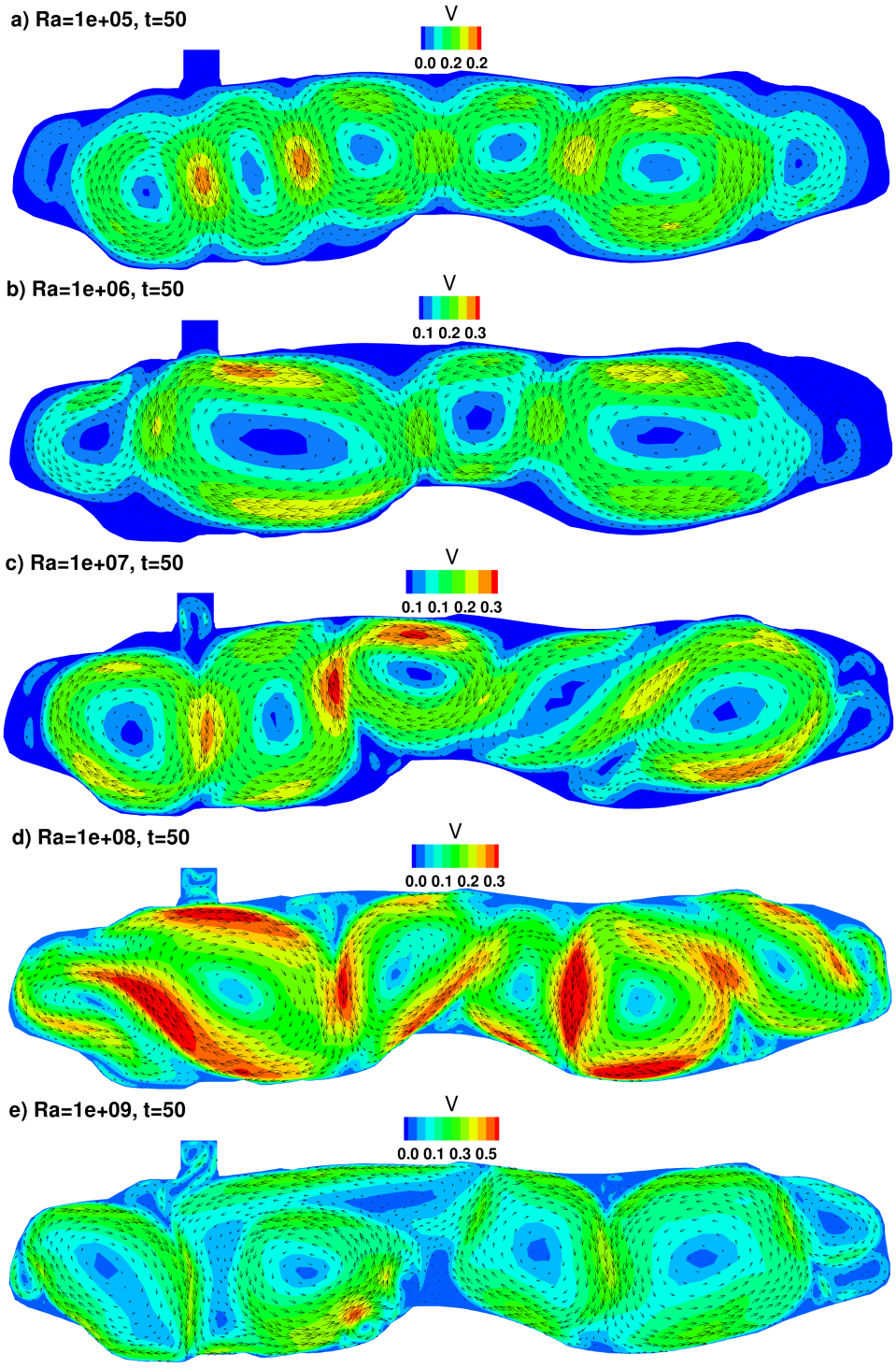

Figure 2: 2D configuration of the Barcq cavity. Snapshots of the natural convection flow at $t = t_f = 50$ for five values of the Rayleigh number. Velocity vectors and contours of the velocity magnitude (colors) showing the presence of convection cells.

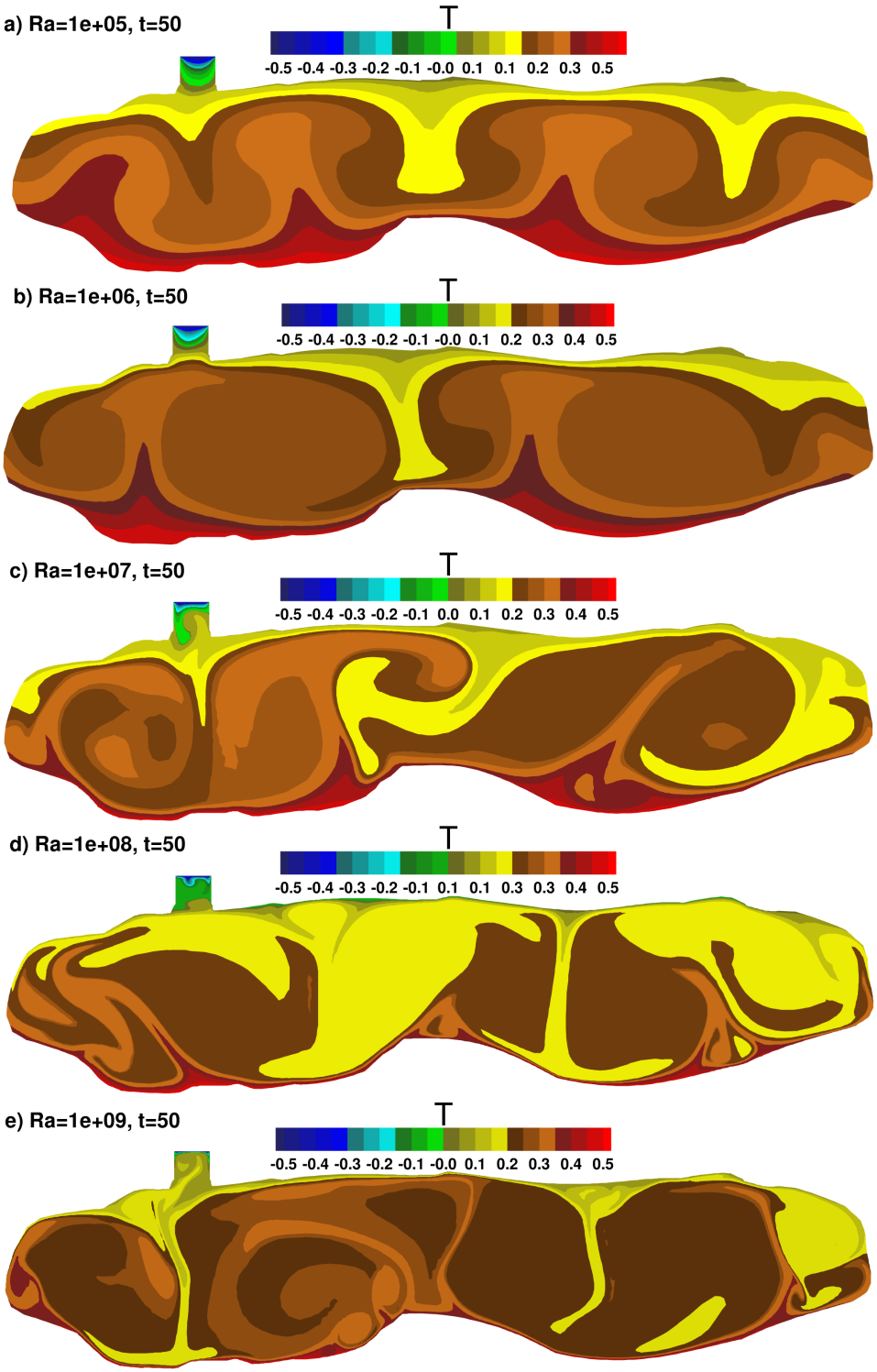

Figure 3: 2D configuration of the Barcq cavity. Snapshots of the natural convection flow at $t = t_f = 50$ for five values of the Rayleigh number. Temperature contours.

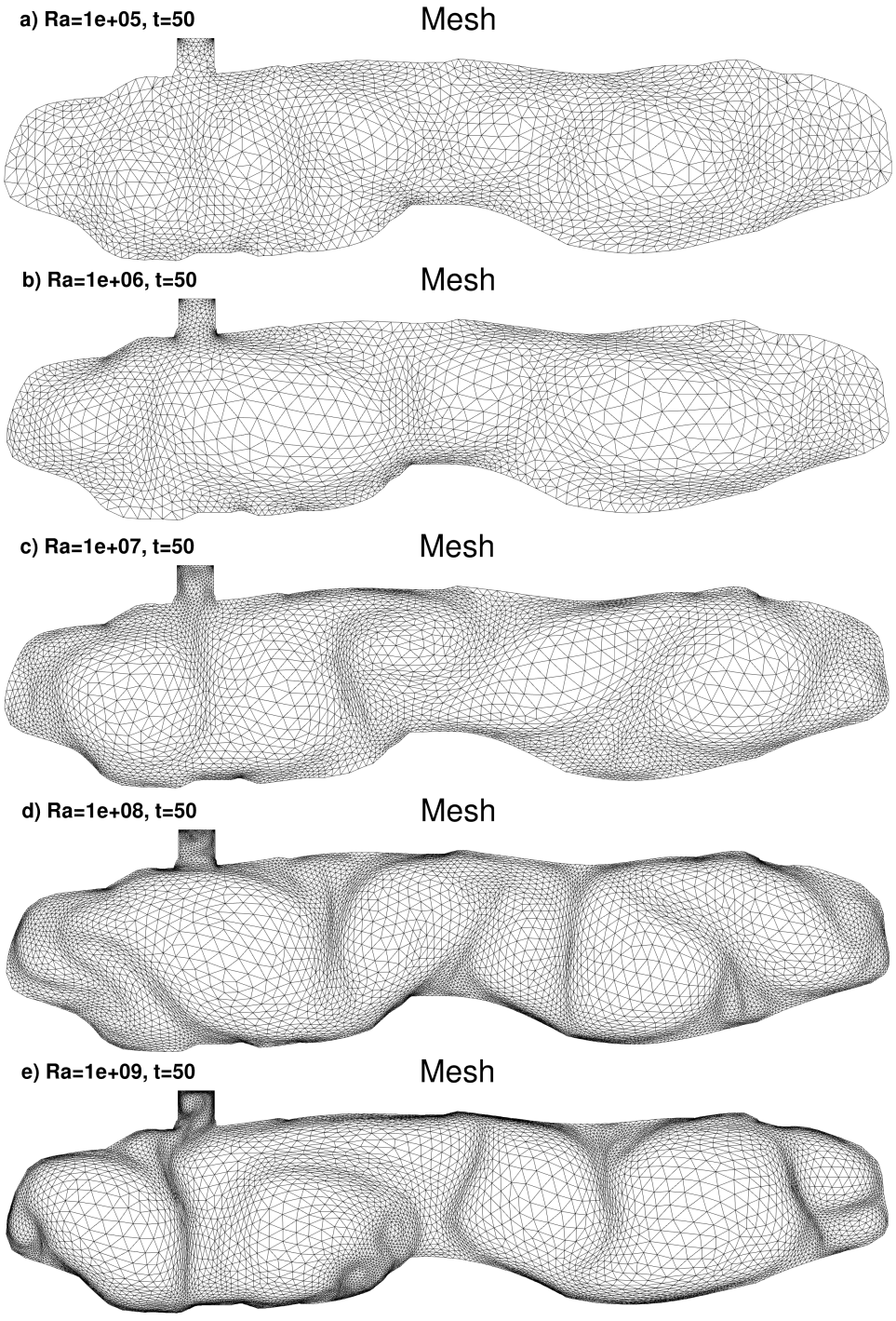

Figure 4: 2D configuration of the Barcq cavity. Adapted finite element mesh at final time $t_f = 450$ and for five values of the Rayleigh number.

To get a better insight on the flow evolution, we show in Fig. 5 the time evolution of the temperature measured at gauges G1 to G4. The gauge G1 is placed at the surface of the well, G2 in the intersection plane between cavity and well, while G3 and G4 are inside in the middle plane of the cavity (see Fig. 1). The curve in Fig. 5a illustrates the time-variation of the temperature at the surface of the well, imposed by the boundary condition (26). Figure 5b, corresponding to the gauge at the bottom of the well, suggests that the convection process initiates at the top of the well by the fall of a cold plume induced by the temperature variation at the surface of the well (gauge G1). This is observed in particular for $\mathcal{R}a = 10^5$ to $\mathcal{R}a = 10^7$, with a minimum of temperature around $t = 5$; the minimum is observed at $t = 10$ for $\mathcal{R}a = 10^8$. During the increase of the top (G1) temperature, the convection tends to weaken within the well: all the curves at G2 follow the same evolution, with similar slopes until the occurrence of the maximum of the top G1 temperature. During the cooling of the well surface, between $t = 25$ and $t = 50$ (see Fig. 5a), more unstable conditions occur within the well (generation of a cold plume at the top). Starting with $t = 25$, the convection evolves differently for each $\mathcal{R}a$ number: as $\mathcal{R}a$ increases, the top cold plume becomes thinner and thinner (see Fig. 3c compared to 3e) and is located along the wall of the well, while a thicker upward flow is induced (see Fig. 2c compared to 2e). As a consequence, the temperature at G2 increases with the $\mathcal{R}a$ number for $t > 25$.

We also note that, starting from $\mathcal{R}a = 10^7$, high frequencies appear within the thermal field, showing the unsteadiness of the convective process. The same observation may be done for gauges G3 and G4 at the interior of the cavity where a large amount of high frequencies are present in the thermal field and high amplitude thermal oscillations are observed. These frequencies are induced by the oscillation of the convective cells that deform during the temperature cycle.

To better quantify the heat transfer at the surface of the well, we show in Fig. 6 the time evolution of the Nusselt number computed at this boundary:

$$\mathcal{N}u = -\int_{L_{well}} \left(\frac{\partial \theta}{\partial y}\right)_{y=y_B} dx. \tag{28}$$

We note an evolution similar to that one obtained in (Sahi, 2016) for the case of natural convection without radiation, which is our case. The heat transfert follows the temperature of gauge G1 placed on top of the well. The Nusselt number usually differs from 1, meaning that a convective flux (either positive or negative) is always present within the well. The lowest values of the Nusselt number are observed for $t = 25$ and for all $\mathcal{R}a$ numbers, *i. e.* in the most unfavourable conditions for the convection process (high temperature at the top). The highest value of $\mathcal{N}u = 15$ is observed for $\mathcal{R}a = 10^9$. The observed peaks highlight significant thermal gradients corresponding to a change in the thermal boundary layer of the cold wall. This phenomenon intensifies with the increase of the Rayleigh number. As an illustration, considering a mean geothermal flux of 60 mW m^{-2} in Normandy, the convective flux associated to the upward flow for $\mathcal{R}a = 10^9$ is equal to 900 mW m^{-2}, which is a high value for the thermal flux.

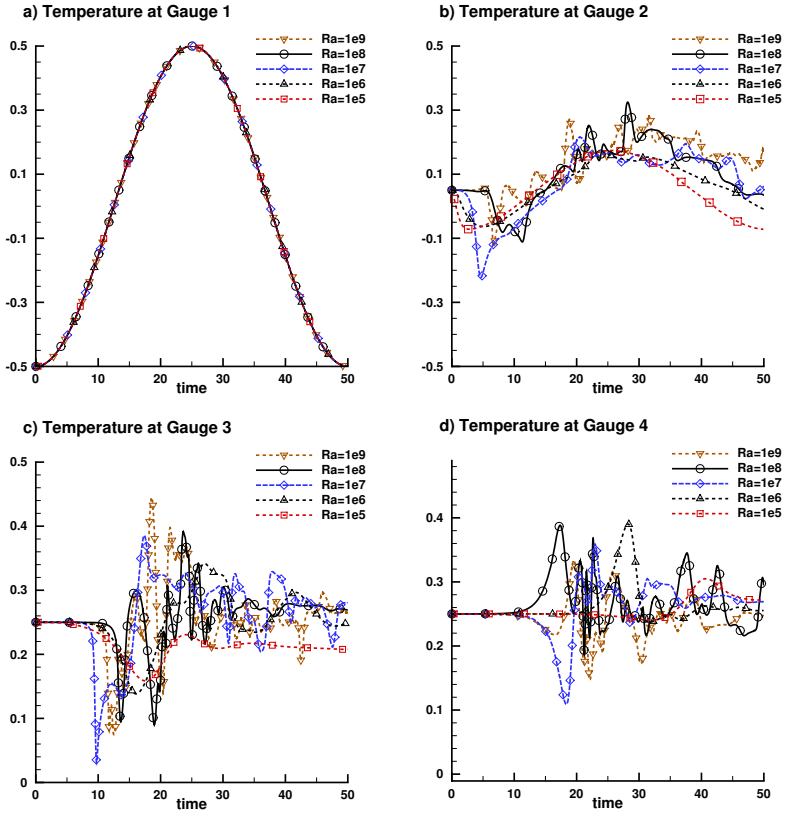

Figure 5: 2D configuration of the Barcq cavity. Time evolution of the temperature measured at gauges G1 to G4 for five values of the Rayleigh number.

3.3.2 Results for the 3D configuration

Computation of the 3D configuration of the Barcq cavity is challenging. As can be seen from Fig. 1, the topology of the cavity is complex, with a narrow part linking the two halves of the cavity. Visualization of the flow is also more involved that in the 2D case. We choose to show in Figs. 7 to 11 four iso-surfaces of temperature and velocity vectors projected on these iso-surfaces. Since the angle of view is slightly varied from one case to another, we present separately the results for the five values of the Rayleigh number.

We first notice that the convective cells are still present, but more disorganized: roll-like cells are visible for $\mathcal{R}a = 10^5$ to 10^7, but are very difficult to characterize for $\mathcal{R}a = 10^8$ to 10^9. Besides, the temperature contrasts observed within the cavity are smaller than for the 2D cases, meaning that the thermal field is more homogeneous. This is due to three-dimensional effects, that also trigger more rapidly a quasi-turbulent state of the flow. High temperature gradients still exist within the well with the presence of hot/cold plumes

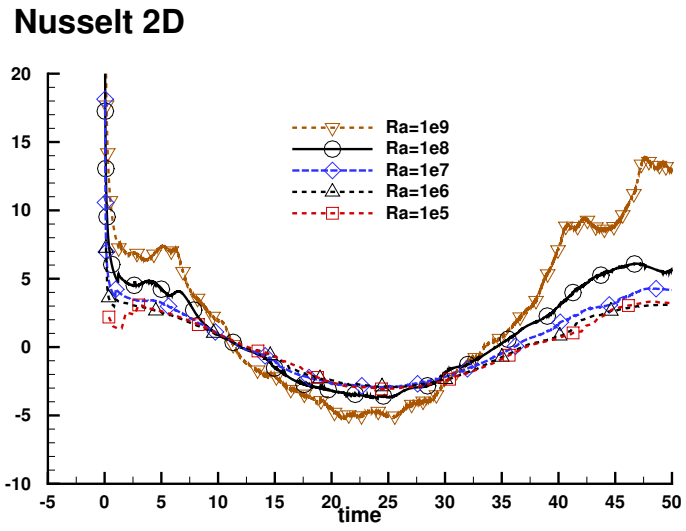

Figure 6: 2D configuration of the Barcq cavity. Time evolution of the Nusselt number computed at the surface of the well ($y = y_b$) for five values of the Rayleigh number.

(Figs. 8, 9 and 10), with a thinning of the top cold plumes as the $\mathcal{R}a$ increases (in a similar way to that observed for the 2D case). For instance, very thin cold plumes can be observed along the wall of the well for $\mathcal{R}a = 10^8$.

As for the 2D configuration, we show in Fig. 12 temperature time-series measured at gauges G1 to G4. In 3D, three gauges are placed in the middle of the horizontal section of the cavity at different depths and one in the middle of the cavity. The temperature at gauge G2 in Fig. 12b do not follow the evolution of the surface signal, as it is located more below the well. The cold plume triggering the convection at the beginning of the calculation (around $t = 10$) and falling down within the cavity is seen by this gauge: its temperature remains quite-stable during the thermal cycle.

Temperatures are higher for $\mathcal{R}a = 10^7$ and 10^8 than for 10^5 and 10^6, but with higher frequencies (in particular for $\mathcal{R}a = 10^8$). Concerning gauges G3 and G4 (Figs. 12c and 12d), high frequencies still occur within the temperature field and the amplitude of the thermal oscillations is lower than for the 2D cases. The Nusselt number (Fig. 13) also follows the temperature cycle for the 3D case. However, its values are much lower than for the 2D case, with the Nusselt number reaching the value of 2 for $\mathcal{R}a = 10^8$. Since the simulation was stopped earlier, the value of the Nusselt number is unknown for $\mathcal{R}a = 10^9$, but we can expect that it will be even higher. Nevertheless, for a Nusselt of 2 and $\mathcal{R}a = 10^8$, the convective flux would be 120 mW m^{-2}, which is a correct value for the flux of geothermal active areas on Earth.

In summary, from a dynamical point of view, the 3D cases share some similarities with

2D calculations: the occurrence of important thermal gradients in the well, the thinning of the top/interior cold plumes inducing large hot air flows. However, important differences appear: i) the 3D geometry tends to disorganize the convective cells from $\mathcal{R}a = 10^8$; ii) 3D effects homogenize the temperature field within the cavity; iii) the value of the Nusselt number is much lower, meaning that the heat released by the convective process at the surface is much lower.

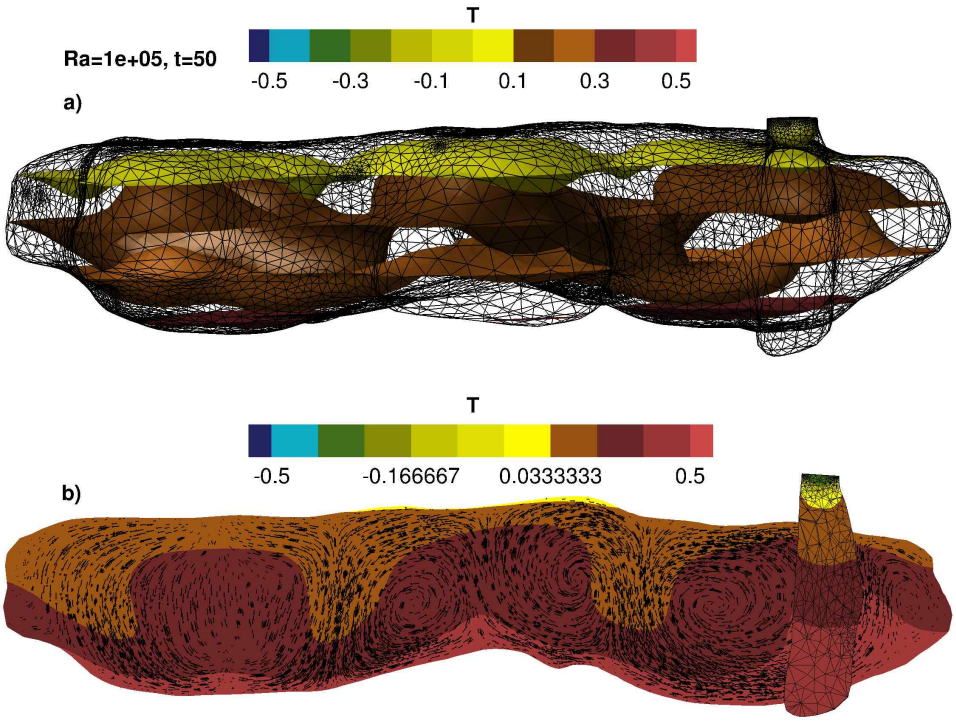

Figure 7: 3D configuration of the Barcq cavity. Snapshot of the natural convection flow at $t = t_f = 50$. a) Mesh and four isosurfaces of temperature, b) velocity vectors. $\mathcal{R}a = 10^5$.

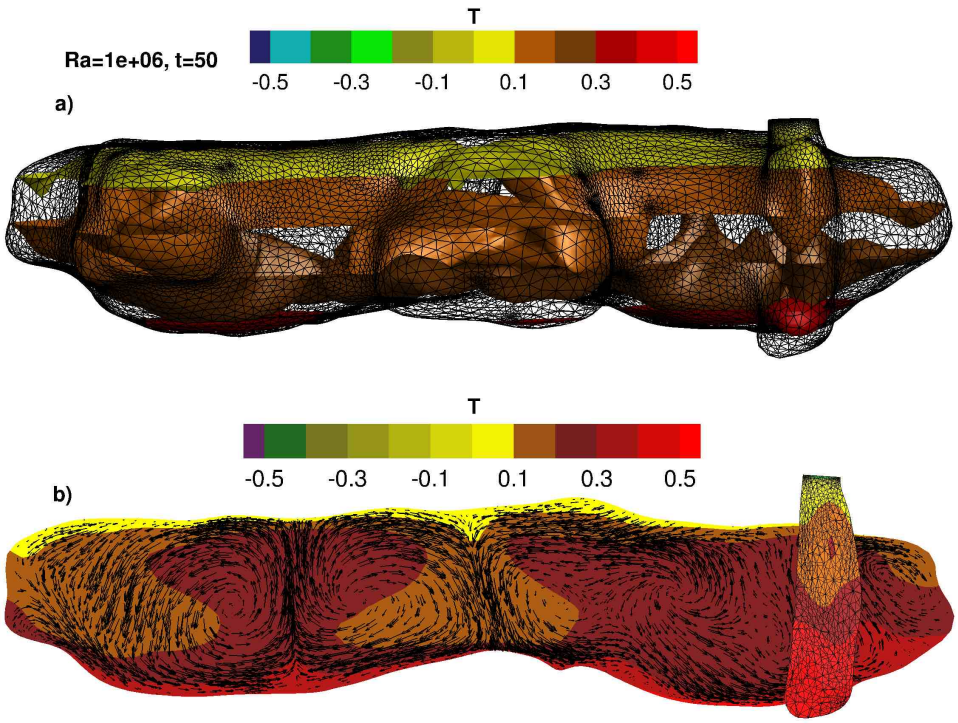

Figure 8: Same caption as for Fig. 7, but for $\mathcal{R}a = 10^6$.

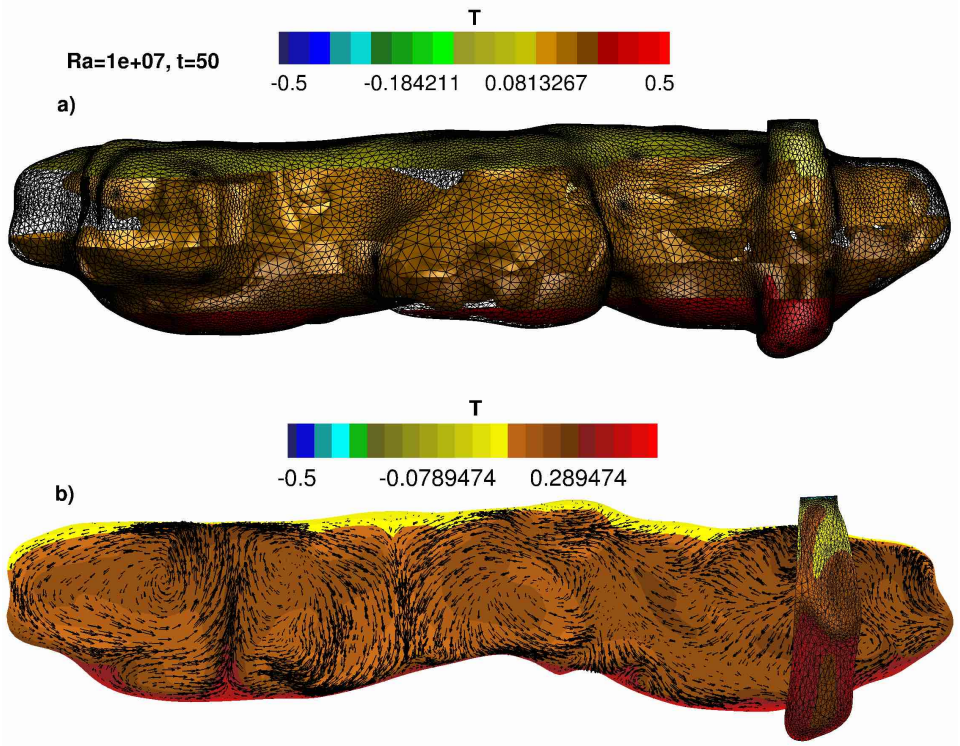

Figure 9: Same caption as for Fig. 7, but for $\mathcal{R}a = 10^7$.

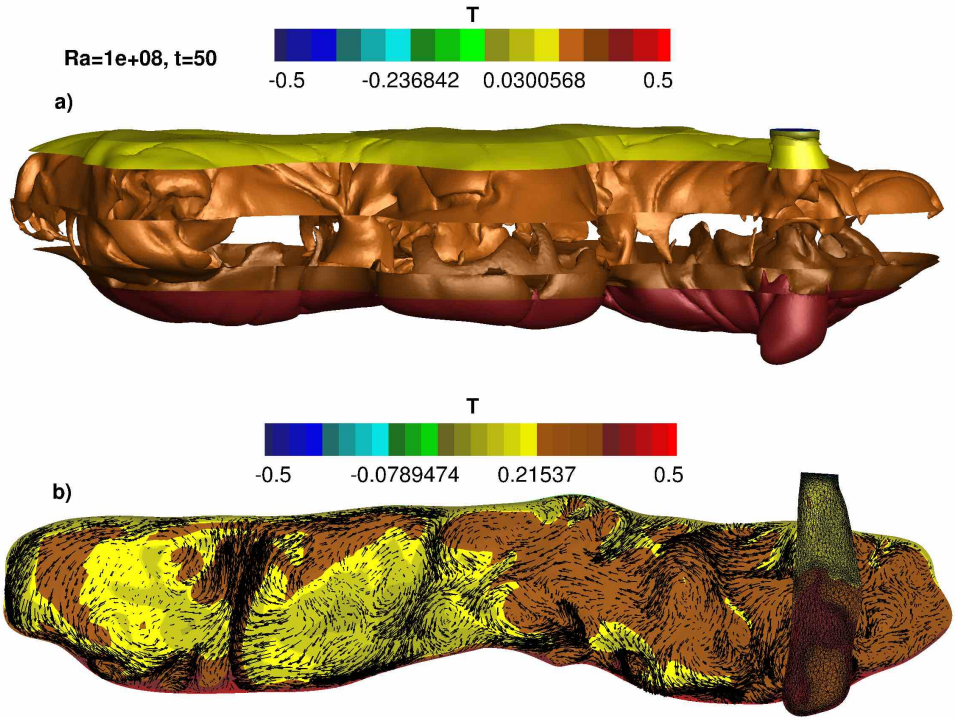

Figure 10: Same caption as for Fig. 7, but for $\mathcal{R}a = 10^8$.

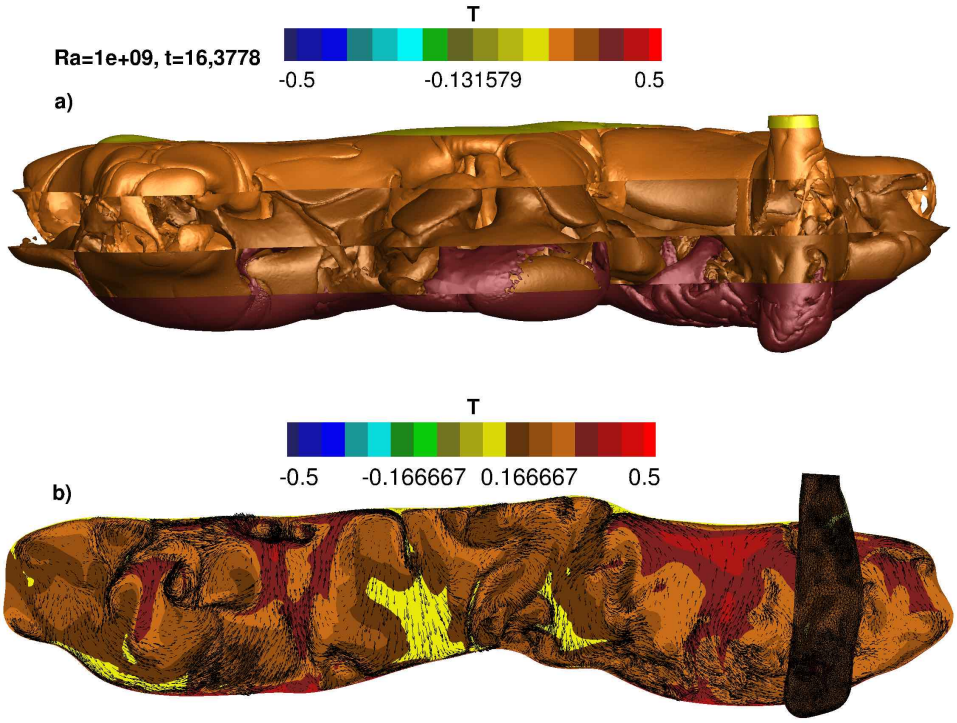

Figure 11: Same caption as for Fig. 7, but for $\mathcal{R}a = 10^8$ and $t = 16 < t_f$.

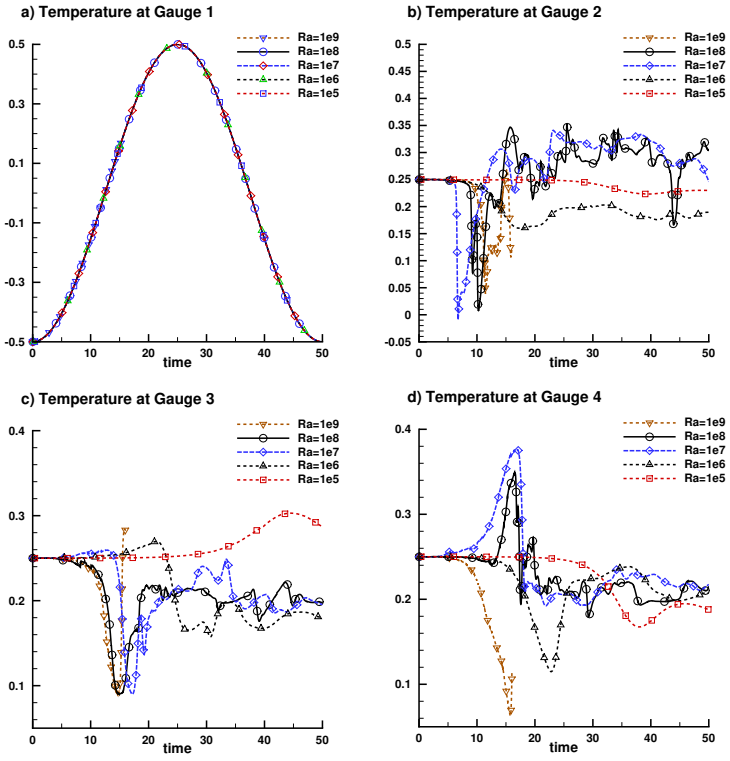

Figure 12: 3D configuration of the Barcq cavity. Time evolution of the temperature measured at gauges G1 to G4 for five values of the Rayleigh number.

4 Summary and conclusions

We presented a numerical model for the thermal behavior of artificial underground cavities. The natural air convection flow was simulated for 2D and 3D geometries corresponding to an actual artificial cavity located at Barcq, in Normandy, France. We first generated the geometry from the 3D points obtained with a photogrammetric method. We then solved the full system of Navier-Stokes equations with Boussinesq approximation for thermal effects. The numerical method is based on a finite element space discretization (triangles in 2D and tetrahedra in 3D) and implemented in FreeFem++ , a free software offering many useful tools (mesh adaptivity, interface with up-to-date libraries like `PETSc`).

The numerical algorithm is original: we used the mini-element P_1^b (P_1-bubble) for velocities and P_1 for the pressure (as opposed to the Taylor-Hood element, commonly used for such problems). For the temperature, we used either P_1 or P_2 finite elements. This discretization allowed us to save computational time, especially for 3D configurations. For the time integration, the Gear scheme offered a second order precision in time. The numer-

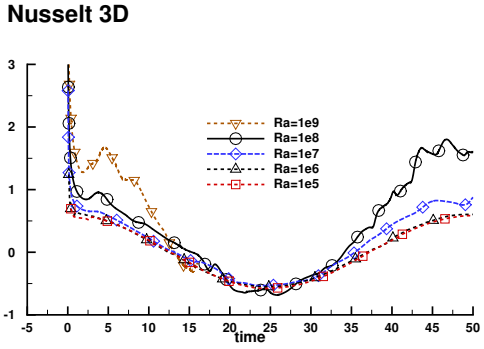

Figure 13: 3D configuration of the Barcq cavity. Time evolution of Nusselt number computed at the surface of the well ($y = y_b$).

ical method was first validated by assessing the space and time convergence rates, using theoretical benchmarks (manufactured solutions). Then we reported 2D and 3D results for the natural convection flow evolution in the Barcq cavity, proving the efficiency of the developed FreeFem++ code.

Numerical simulations were performed for Rayleigh numbers ranging from 10^5 to 10^9. We presented snapshots of the velocity and temperature fields, and also time series of temperature measures at four gauges. The results showed that: i) the natural convection of air in an empty cavity can be triggered by important variations of the temperature at the surface of the well; ii) the number of convection cells is geometry dependent and the thermal gradients play the most important role in the heat transfer; iii) the airflow velocity and of the temperature gradients within the well become intense for high Rayleigh numbers ($\mathcal{R}a > 10^7$), which makes possible the detection of the wells by spotting temperature contrasts at the surface; iv) the computed values of the Nusselt number at the well surface suggest that natural convection potentially absorb or release heat from the atmosphere.

We also simulated 3D cases, which are computationally challenging. For the 3D geometry and $\mathcal{R}a > 10^8$, the convection is much more disorganized and the temperature tends to be more homogeneous than in the 2D geometry. However, the well is still affected by temperature gradients generated by the time-oscillating surface temperature. We also observed that, although it takes much lower values than in the 2D case, the Nusselt number for the 3D case is still important, if compared to usual values of the heat flux range on Earth.

Further work will concern a more realistic model for the study of the thermal behavior of cavities by: i) including a porous medium model describing the geological environment around the cavity; ii) considering the presence of solid materials blocking the well; iii) taking into account the radiation at the surface of the well. The final purpose of this study is to use thermal infrared images taken by drones to detect cavities with blocked wells by identifying thermal anomalies at the surface.

Acknowledgments

Part of this work used computational resources provided by CRIANN (Centre Régional Informatique et d'Applications Numériques de Normandie).

Appendix A Space and time accuracy of the method. Tests using manufactured solutions.

A.1 Rate of convergence in space

To compute the convergence in space of our numerical method we used the Burggraf manufactured solution. This exact solution corresponds to a time-independent recirculating flow inside a square cavity $[0,1]\times[0,1]$. This flow is similar to the well-known entrained cavity flow, with the difference that the velocity singularity at the top corners of the cavity is avoided. The cavity is transformed in a differentially heated cavity (see also Rakotondrandisa et al., 2020) by imposing the temperatures of lateral walls (T_{hot} and T_{cold}, respectively); the upper and lower walls are adiabatic. The expressions for the two components of the velocity, the pressure and temperature are as follows:

$$
\begin{aligned}
&u_1(x,y) = \sigma g'(x)h'(y),\\
&u_2(x,y) = -\sigma g''(x)h(y),\\
&p(x,y) = \frac{\sigma}{Re}(h^{(3)}(y)g(x) + g''(x)h'(y)) + \frac{\sigma^2}{2}g'(x)^2(h(y)h''(y) - h'^2(y),\\
&\theta(x,y) = T_{cold} + (T_{hot} - T_{cold})y + a(x)b(y),
\end{aligned}
$$

with $\sigma \geq 0$ am amplitude parameter and functions:

$$
\begin{aligned}
g(x) &= \frac{x^5}{5} - \frac{x^4}{2} + \frac{x^3}{3},\\
h(y) &= y^4 - y^2,\\
a(x) &= cos(\pi x),\\
b(y) &= y(1-y).
\end{aligned}
$$

Note that $\theta_x(x,y) = a'(x)b(y), \theta_y(x,y) = T_{hot} - T_{cold} + a(x)b'(y)$, $\theta_{xx}(x,y) = a''(x)b(y)$ and $\theta_{yy}(x,y) = a(x)b''(y)$.

If we plug this solution in the system of equations (1)-(3), we obtain the following right-hand-side terms:

$$
\begin{aligned}
f_{u_1} &= 0\\
f_{u_2} &= \sigma^2 h(y)h'(y)(g''^2(x) - g'(x)g^{(3)}(x)) + \frac{\sigma}{\mathcal{R}e}(h^{(4)}(y)g(x) + 2g''(x)h''(y) + g^{(4)}(x)h(y))\\
&\quad + \frac{\sigma^2}{2}g'^2(x)(h(y)h^{(3)} - h'(y)h''(y)) - f_B(\theta) \qquad (29)\\
f_\theta &= u_1\theta_x + u_2\theta_y - \frac{1}{\mathcal{R}e\mathcal{P}r}(\theta_{xx} + \theta_{yy}) \qquad (30)
\end{aligned}
$$

We thus solve the system (1)-(3) with right-hand-side terms (30) to assess on the convergence rate of the method in space. Errors are measured in natural norms: H^1-norm for the velocity components u_1, u_2 and temperature θ, and L^2-norm for the pressure p. Figures A.1(a,b) correspond to the simulation using P_1 finite elements for the temperature, while in Fig. A.1(c,d) P_2 finite elements were used for the temperature. We recover the expected orders of convergence: first order ($\mathcal{O}(h)$) convergence for velocity and first or second order ($\mathcal{O}(h^2)$) convergence for the temperature (depending if P_1 or P_2 are used). Theoretical second order convergence is obtained for pressure (recall that this is measured using the L^2-norm). Space convergence rates were confirmed for the 3D configuration of the same Burggraf solution, as shown in Fig. A.1.

A.1.1 Rate of convergence in time

To compute the convergence in time for the natural convection without radiation, we used the Nourgaliev Nourgaliev et al. (2016) exact solution (see also Rakotondrandisa et al., 2020):

$$
\begin{aligned}
u_1(x,y,t) &= (\delta U_0 + \alpha_u sin(t))cos(x+\gamma_1 t)sin(y+\gamma_2 t),\\
u_2(x,y,t) &= -(\delta U_0 + \alpha_u sin(t))sin(x+\gamma_1 t)cos(y+\gamma_2 t),\\
p(x,y,t) &= \bar{P} + (\delta P_0 + \alpha_p sint(t))sin(x+\gamma_1 t)cos(y+\gamma_2 t),\\
\theta(x,y,t) &= \bar{\theta} + (\delta t_0 + \alpha_t sint(t))cos(x+\gamma_1 t)sin(y+\gamma_2 t).
\end{aligned}
$$

with:

$$\gamma_1 = \gamma_2 = 1, \bar{P} = 0, \bar{\theta} = 1, \delta t_0 = \delta U_0 = 1, \delta P_0 = 0.1, \alpha_P = 0.05, \alpha_u = 0.4, \alpha_t = 0.1.$$

For the right-hand-side member of the system of equations (1)-(3) we obtain:

$$
\begin{aligned}
f_{u_1} = \alpha_u cos(t)cos(a)sin(b) - U_c\gamma_1 sin(a)sin(b) + U_c\gamma_2 cos(a)cos(b)\\
-U_c u_1(x,y,t)sin(a)sin(b) + U_c u_2(x,y,t)cos(a)cos(b) + P_c sin(a)sin(b)\\
+\frac{2}{\mathcal{R}e}u_1(x,y,t),\\
f_{u_2} = -\alpha_u cos(t)sin(a)cos(b) - U_c\gamma_1 cos(a)cos(b) + U_c\gamma_2 sin(a)sin(b)\\
-U_c u_1(x,y,t)cos(a)cos(b) + U_c u_2(x,y,t)sin(a)sin(b) - P_c sin(a)sin(b)\\
+\frac{2}{\mathcal{R}e}u_2(x,y,t) - f_B(\theta),\\
f_\theta = \alpha_t cos(t)cos(a)sin(b) - T_c\gamma_1 sin(a)sin(b) + T_c\gamma_2 cos(a)cos(b)\\
-T_c u_1(x,y,t)sin(a)sin(b) + T_c u_2(x,y,t)cos(a)cos(b)\\
+\frac{2}{\mathcal{R}e\mathcal{P}r}T_{2c}(x,y,t)cos(a)sin(b).
\end{aligned}
$$

where $a = (x+\gamma_1 t)$, $b = (y+\gamma_2 t)$ and $U_c = (\delta U_0 + \alpha_u \sin(t))$, $T_c = (\delta T_0 + \alpha_u \sin(t))$, $P_c = (\delta P_0 + \alpha_u \sin(t))$.

Using the study for the time accuracy, we first ixed the grid size to $h = \delta x = 0.01$ in 2D and $h = \delta x = 0.02$ in 3D to ensure small spatial discretization errors. We then used P_1 or P_2 finite elements for the temperature. For diminishing values of the time step δt, the solution was evolved in time up to the time instant $t_{max} = \pi$ at which the error was computed. For the 2D cavity, the time convergence rates for temperature and the total velocity $u = \sqrt{u_1^2 + u_2^2}$ are displayed in Figs. 16(a, b). For both computations, using for the temperature either P_1 or P_2 finite elements, the expected second order in time is obtained. Figure 17 shows the same second-order convergence rate for the 3D case.

Appendix B Computation details and performance of the solver

B.1 PETSc solvers

The performance of the code was assessed by simulating the natural convention in the Barcq cavity. Linear systems in the Newton method were solved with the PETSc library. For all simulations we used the following parameters:

- for the 2D case we used a direct LU method with parameters in PETSc: `"-pc_type lu -ksp_type preonly"`;
- for the 3D problem, we used the following options: `"-ksp_converged_reason -pc_type asm -pc_asm_overlap 1 -ksp_pc_side left -ksp_type gmres -ksp_gmres_restart 50 -ksp_max_it 100 -ksp_atol 1e-5 -sub_pc_type lu -sub_pc_factor_mat_solver_type mumps -ksp_rtol 1e-6"`.

B.2 Computational resources for 2D and 3D simulations

Tables 1 and 2 show that necessary computational resources strongly depend on the value of the Rayleigh $\mathcal{R}a$ number. With increasing value of the $\mathcal{R}a$ number, the gradients of velocity and temperature are more important and the mesh refinement procedure produces denser meshes. The variation in time of the number of degrees of freedom due to mesh adaptivity/refinement is presented in Fig. 18. The mesh is dynamically refined in regions of high gradients and coarsened in regions of low gradients.

Using a medium-size parallel computer, 2D simulations are affordable for all range of $\mathcal{R}a$ numbers, with a reasonable computational time (see Tab. 1). For the 3D configuration at the highest value $\mathcal{R}a = 10^9$ the flow generates smaller and smaller structures and the mesh refinement results in a very dense mesh requiring a huge amount of memory and CPU time to solve associated linear systems. This is the reason why this 3D case was stopped at $t = 16 < \lambda = 50$ (see Tab. 2). Further optimizations on the use of the PETSc solvers (finding good preconditionners) and larger computers are necessary to simulate this case over an entire time period.

Case	CPU (min)	max number of triangles	number of time steps
$\mathcal{R}a = 10^5$	1	4 305	133
$\mathcal{R}a = 10^6$	3	6 564	421
$\mathcal{R}a = 10^7$	11	12 499	1 332
$\mathcal{R}a = 10^8$	57	20 965	4 213
$\mathcal{R}a = 10^9$	240	28 888	4 364

Table 1: Computational resources for 2D simulations. For all simulations, we used 6 processors and stopped the calculation at the final time $t_f = 50$. We report the total CPU time (in minutes), the maximum number of triangles after the mesh adaptation and the number of time steps.

Case	t_f	CPU (h)	processors	memory (GB)	max number of triangles	number of time steps
$\mathcal{R}a = 10^5$	50	2	28	22	320 623	133
$\mathcal{R}a = 10^6$	50	10	56	85	685 503	421
$\mathcal{R}a = 10^7$	50	72	108	279	2 507 179	1 332
$\mathcal{R}a = 10^8$	50	314	209	1790	8 685 939	4 213
$\mathcal{R}a = 10^9$	16	263	207	4540	18 959 948	4 364

Table 2: Computational resources for 3D simulations. We report the final time t_f, the total CPU time (in hours), the number of processors used for the computation, the amount of necessary memory (in GB), the maximum number of triangles after the mesh adaptation and the number of time steps. Note that the 3D simulation for the case $\mathcal{R}a = 10^9$ was stopped earlier.

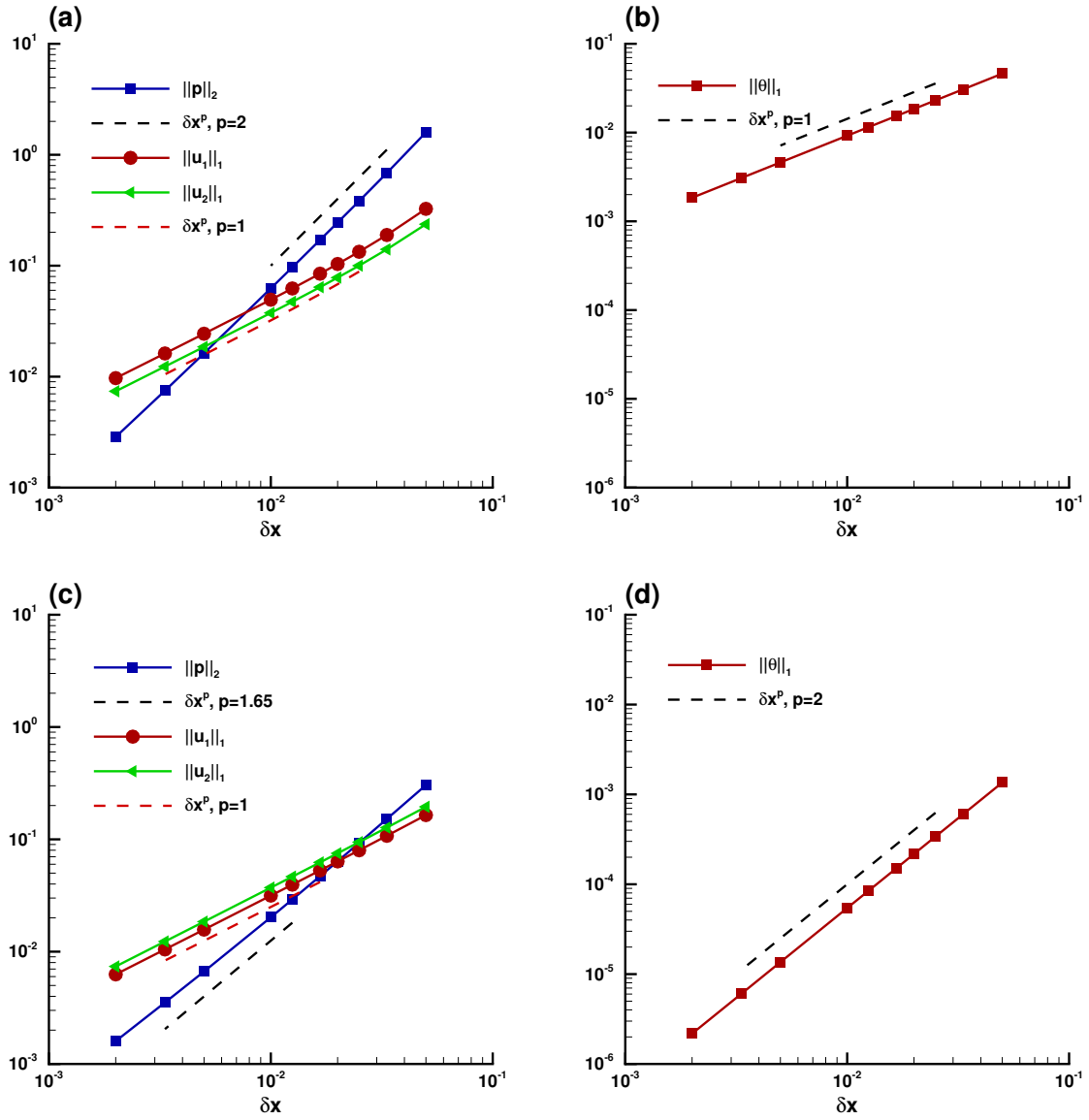

Figure 14: Space convergence of the numerical method tested using the 2D Burggraf manufactured solution. The global error was computed using natural norms: L2-norm for the pressure p and H_1-norm for velocity components u_1, u_2 and temperature θ. P_{1b}/P_1 finite elements are used for the velocity and pressure respectively. Discretization of the temperature using P_1 (plots a and b) and P_2 (plots c and d) finite elements.

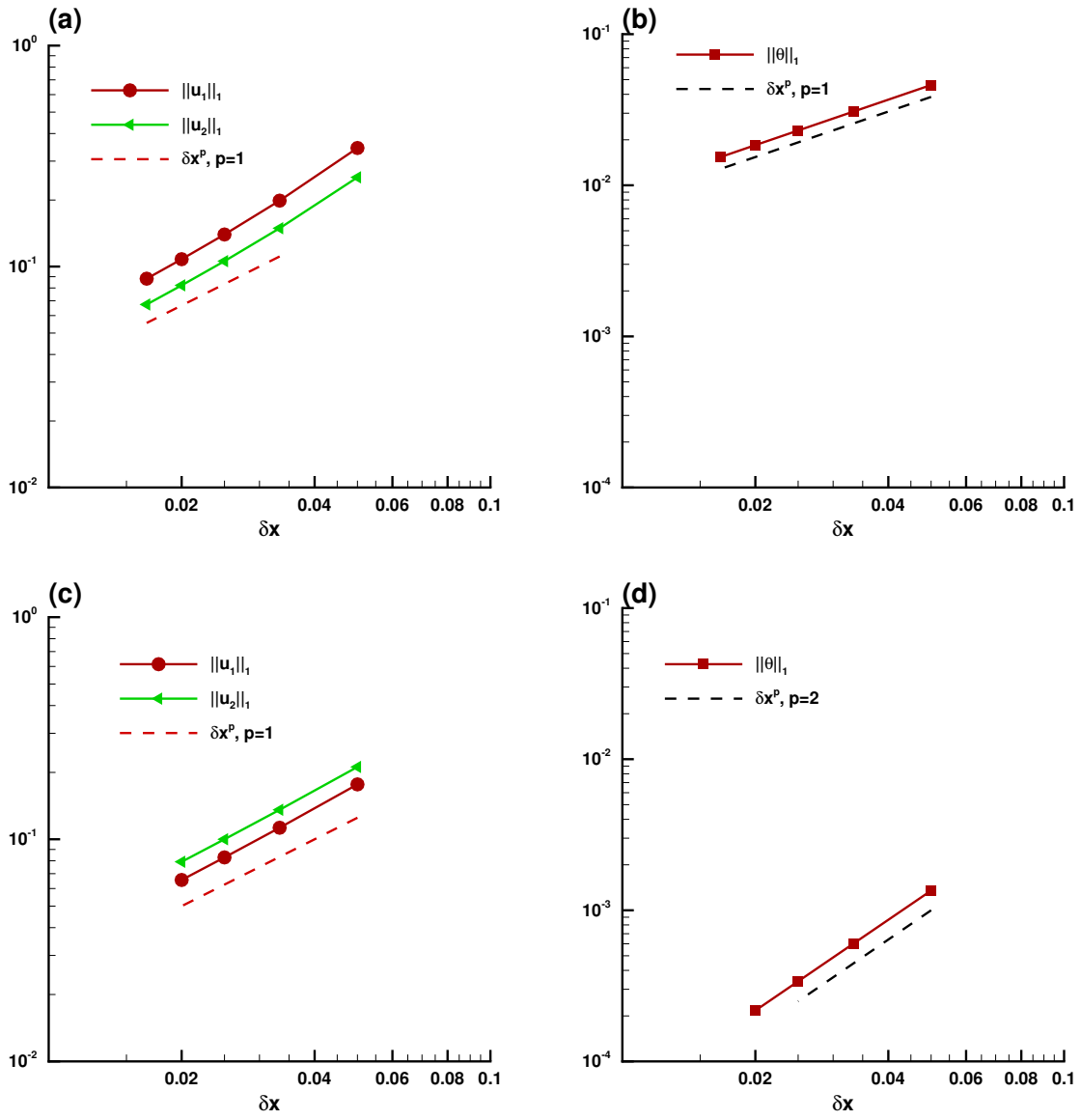

Figure 15: Same caption as for Fig. A.1, but for the 3D Burggraf manufactured solution.

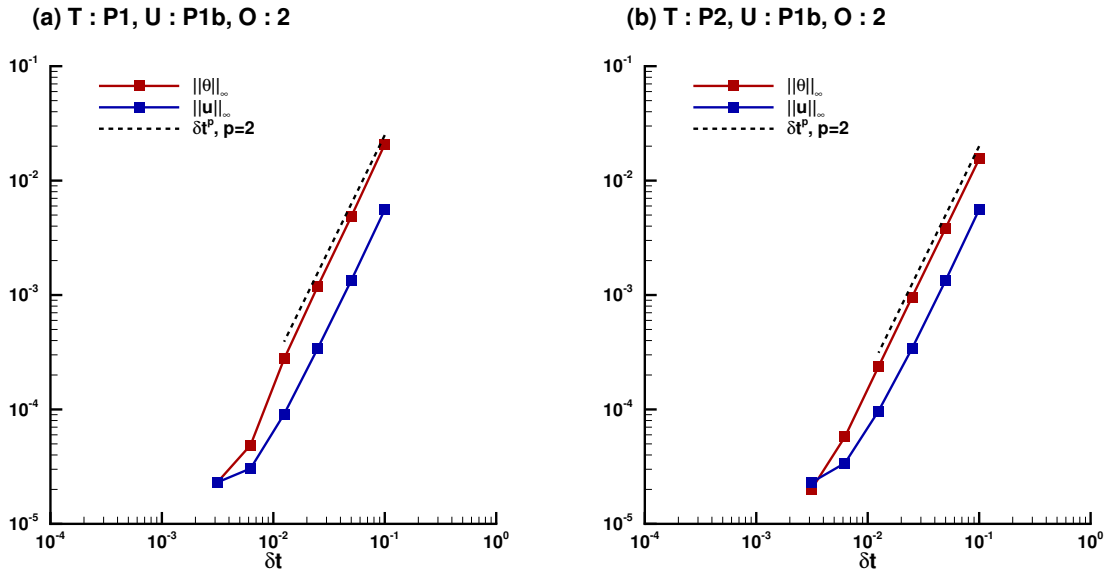

Figure 16: Time convergence of the numerical method tested using the 2D Nourgaliev manufactured solution. a) P_1 finite element for the temperature, b) P_2 finite element for the temperature.

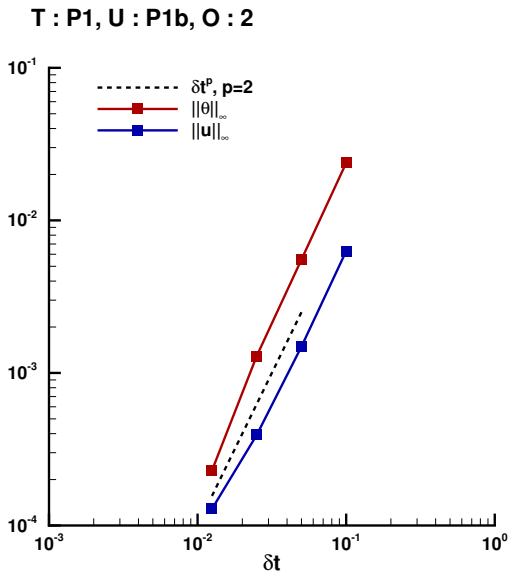

Figure 17: Same caption as for Fig. 16, but for the 3D Nourgaliev manufactured solution. P_1 finite element for the temperature.

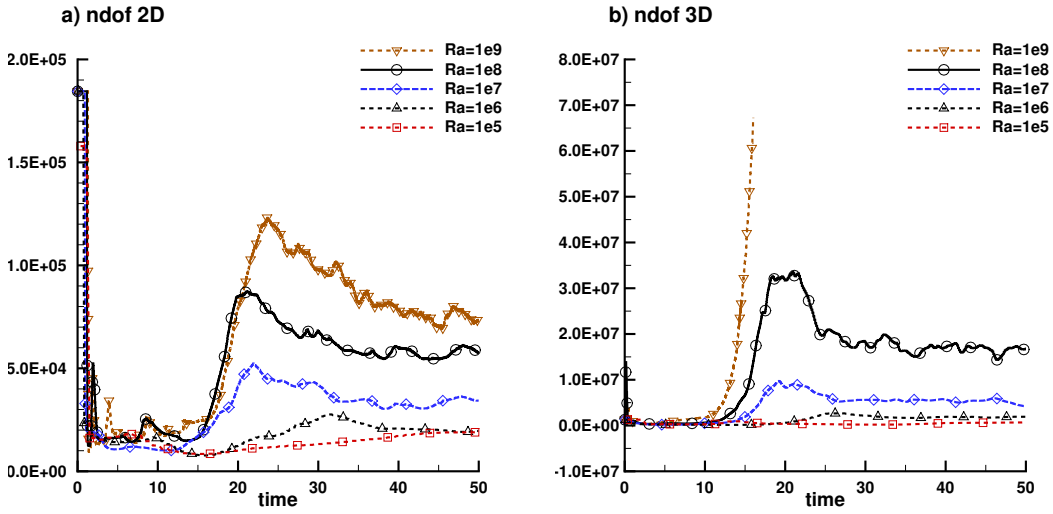

Figure 18: Variation in time of the number of degrees of freedom (ndof) due to mesh adaptivity/refinement. a) 2D simulations, b) 3D simulations.

References

A. M. Youssef, Y. A. Zabramwi, F. Gutiérrez, A. M. Bahamil, Z. A. Otaibi, A. J. Zahrani, Sinkholes induced by uncontrolled groundwater withdrawal for agriculture in Arid Saudi Arabia. Integration of remote-sensing and geophysical (ERT) techniques, Journal of Arid Environments 177 (2020) 104132.

E. J. Lee, S. Y. Shin, B. C. Ko, C. Chang, Early sinkhole detection using a drone-based thermal camera and image processing, Infrared Physics & Technology 78 (2016) 223–232.

H. Xiao, Y. J. Kim, B. H. Nam, D. Wang, Investigation of the impacts of local-scale hydrogeologic conditions on sinkhole occurrence in East-Central florida, USA, Environmental Earth Sciences 75 (2016) 1–16.

D. Closson, N. A. Karaki, Y. Klinger, M. J. Hussein, Subsidence and sinkhole hazard assessment in the southern Dead Sea area, Jordan, Pure and Applied geophysics 162 (2005) 221–248.

S. Kruse, M. Grasmueck, M. Weiss, D. Viggiano, Sinkhole structure imaging in covered Karst terrain, Geophysical Research Letters 33 (2006).

D. Carbonel, V. Rodríguez, F. Gutiérrez, J. P. McCalpin, R. Linares, C. Roqué, M. Zarroca, J. Guerrero, I. Sasowsky, Evaluation of trenching, ground penetrating radar (GPR) and electrical resistivity tomography (ERT) for sinkhole characterization, Earth Surface Processes and Landforms 39 (2014) 214–227.

K. T. Tran, M. McVay, M. Faraone, D. Horhota, Sinkhole detection using 2d full seismic waveform tomography, Geophysics 78 (2013) R175–R183.

A. Kulshrestha, L. Chang, A. Stein, Sinkhole scanner: A new method to detect sinkhole-related spatio-temporal patterns in InSAR deformation time series, Remote sensing 13 (2021) 2906.

G. Saracino, L. Amato, F. Ambrosino, G. Antonucci, L. Bonechi, L. Cimmino, L. Consiglio, R. Alessandro, E. D. Luzio, G. Minin, et al., Imaging of underground cavities with cosmic-ray muons from observations at Mt. Echia (Naples), Scientific reports 7 (2017) 1181.

K. Morishima, M. Kuno, A. Nishio, N. Kitagawa, Y. Manabe, M. Moto, F. Takasaki, H. Fujii, K. Satoh, H. Kodama, et al., Discovery of a big void in Khufu's Pyramid by observation of cosmic-ray muons, Nature 552 (2017) 386–390.

A. Philippe, L. Dore, P. Azemard, F. Gaumet, D. Virely, Utilisation des paramètres combinés de forages dans les études de recherche de cavités souterraines anthropiques, in: 11èmes journées nationales de géotechnique et de géologie de l'ingénieur, 2022.

A. Benito-Calvo, F. Gutiérrez, A. Martínez-Fernández, D. Carbonel, T. Karampaglidis, G. Desir, J. Sevil, J. Guerrero, I. Fabregat, Á. García-Arnay, 4d monitoring of active

sinkholes with a terrestrial laser scanner (TLS): a case study in the evaporite karst of the Ebro valley, NE Spain, Remote Sensing 10 (2018) 571.

R. Antoine, C. Fauchard, J.-F. Oehler, P. Joignant, Permeability and voids influence on the thermal signal, as inferred by multitemporal UAV-based infrared and visible images, Journal of Hydrology 587 (2020) 124907.

A. Cooper, Airborne multispectral scanning of subsidence caused by Permian gypsum dissolution at Ripon, North Yorkshire, Quarterly Journal of Engineering Geology and Hydrogeology 22 (1989) 219–229.

J. J. Wynne, T. N. Titus, G. C. Diaz, On developing thermal cave detection techniques for Earth, the Moon and Mars, Earth and Planetary Science Letters 272 (2008) 240–250.

J. L. Perez-Garcia, M. Sánchez-Gómez, J. M. Gómez-López, T. Guerra, D. Gil, T. Fernández, Georeferenced thermal infrared images from UAV surveys as a potential tool to detect and characterize shallow cave ducts, Engineering Geology 246 (2018) 277–287.

E. P. Carreño-Alvarado, D. Ayala-Cabrera, R. Pérez-García, J. Izquierdo, Identification of buried pipes using thermal images and data mining, Procedia Engineering 89 (2014) 1445–1451.

T. Lopez, R. Antoine, D. Baratoux, M. Rabinowicz, K. Kurita, L. d'Uston, Thermal anomalies on pit craters and sinuous rilles of Arsia Mons: Possible signatures of atmospheric gas circulation in the volcano, Journal of Geophysical Research: Planets 117 (2012).

C. Adam, E. Manier, N. Berenger, J. Durville, H. De Solere, F. Moronval, F. Hedou, Les marnières de Haute-Normandie Méthodologies d'étude et de prévention, Technical Report, Guide technique- Laboratoire central des Ponts et Chaussées, 2008.

C. Fauchard, P. Pothérat, Détection de cavités souterraines par méthodes géophysiques, guide technique, 2004.

R. H. Buecher, et al., Microclimate study of Kartchner caverns, Arizona, Journal of Cave and Karst Studies 61 (1999) 108–120.

J. Wilson, S. Tyler, A. Jorgensen, R. Dwivedi, P. Boston, P. Burger, Sensing turbulent flow and heat transport in a cave conduit, EOS Transactions AGU 89 (2008) 4–5.

T. Wigley, C. Brown, Geophysical applications of heat and mass transfer in turbulent pipe flow, Boundary-layer meteorology 1 (1971) 300–320.

R. Dwivedi, Modeling and field study of cave micrometeorology: Role of natural convection, Ph.D. thesis, New Mexico Institute of Mining and Technology, 2010.

R. Temam, Navier-Stokes equations and nonlinear functional analysis, SIAM, Philadelphia, 1983.

V. Girault, P.-A. Raviart, Finite element methods for Navier-Stokes equations, Springer Verlag, Berlin, 1986.

A. Quarteroni, A. Valli, Numerical Approximation of Partial Differential Equations, Springer-Verlag, Berlin and Heidelberg, 1994.

A. Rakotondrandisa, G. Sadaka, I. Danaila, A finite-element toolbox for the simulation of solid-liquid phase-change systems with natural convection, Computer Physics Communications 253 (2020) 107188.

G. Sadaka, A. Rakotondrandisa, P.-H. Tournier, F. Luddens, C. Lothodé, I. Danaila, Parallel finite-element codes for the simulation of two-dimensional and three-dimensional solid-liquid phase-change systems with natural convection, Computer Physics Communications 257 (2020) 107492.

Y. Belhamadia, A. S. Kane, A. Fortin, An enhanced mathematical model for phase change problems with natural convection, International Journal of Numerical Analysis and Modeling 3 (2012) 192–206.

C. Legrand, F. Luddens, I. Danaila, On the convergence of a low order Lagrange finite element approach for natural convection problems, Computers & Mathematics with Applications 147 (2023) 259–277.

D. N. Arnold, F. Brezzi, M. Fortin, A stable finite element for the Stokes equations, Calcolo 21 (1984) 337–344.

F. Brezzi, M. Fortin, Mixed and hybrid finite element methods, Springer Verlag, 1991.

P. J. Roache, Verification and Validation in Computational Science and Engineering, Hermosa Publishers, 1998.

C. Fauchard, R. Antoine, F. Bretar, J. Lacogne, Y. Fargier, C. Maisonnave, V. Guilbert, P. Marjerie, P.-F. Thérain, J.-P. Dupont, M. Pierrot-Deseilligny, Assessment of an ancient bridge combining geophysical and advanced photogrammetric methods: Application to the Pont De Coq, France, Journal of Applied Geophysics 98 (2013) 100–112.

F. Hecht, New developments in Freefem++, Journal of Numerical Mathematics 20 (2012) 251–266.

C. Dapogny, C. Dobrzynski, P. Frey, Three-dimensional adaptive domain remeshing, implicit domain meshing, and applications to free and moving boundary problems, Journal of Computational Physics 262 (2014) 358 – 378.

S. Balay, S. Abhyankar, S. Benson, J. Brown, P. R. Brune, K. R. Buschelman, E. Constantinescu, A. Dener, J. Faibussowitsch, W. D. Gropp, et al., PETSc/TAO users manual, Technical Report, Argonne National Lab.(ANL), Argonne, IL (United States), 2022.

A. Sahi, Modélisation et simulation numérique des transferts thermiques dans les cavités fines avec parois complexe en présences d'un fluide classique, Ph.D. thesis, Université Abderrahmane Mira - Bejaia, 2016.

R. Nourgaliev, H. Luo, B. Weston, A. Anderson, S. Schofield, T. Dunn, J.-P. Delplanque, Fully-implicit orthogonal reconstructed discontinuous galerkin method for fluid dynamics with phase change, Journal of Computational Physics 305 (2016) 964–996.